J. Fluid Mech. (2023), *vol*. 957, A13, doi:10.1017/jfm.2022.1026

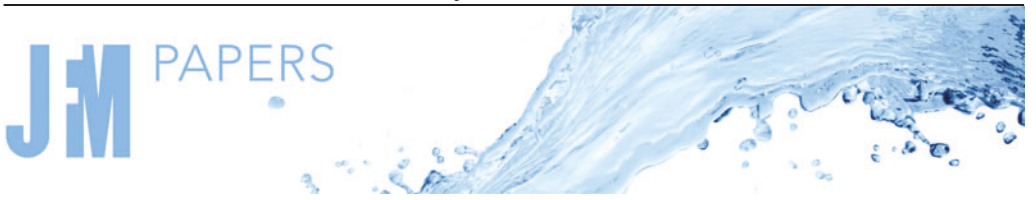

Single sidewall cooling modulation on Rayleigh–Bénard convection

Soohyeon Kang[1], Shyuan Cheng[1], Liu Hong[1], Jin-Tae Kim[1] and Leonardo P. Chamorro[1,2,3,4,†]

[1]Mechanical Science and Engineering, University of Illinois, Urbana, IL 61801

[2]Geology, University of Illinois, Urbana, IL 61801

[3]Civil and Environmental Engineering, University of Illinois, Urbana, IL 61801

[4]Aerospace Engineering, University of Illinois, Urbana, IL 61801

(Received 26 June 2022; revised 19 October 2022; accepted 1 December 2022)

We experimentally explored the effect of single-sidewall cooling on Rayleigh–Bénard (RB) convection. Canonical RB was also studied to aid insight. The scenarios shared tank dimensions and bottom and top wall temperatures; the single sidewall cooling had the top wall temperature. Turbulence was explored at two canonical Rayleigh numbers, $Ra = 1.6 \times 10^{10}$ and $Ra = 2 \times 10^{9}$ under Prandtl number $Pr = 5.4$. Particle image velocimetry described vertical planes parallel and perpendicular to the sidewall cooling. The two Ra scenarios reveal pronounced changes in the flow structure and large-scale circulation (LSC) due to the sidewall cooling. The density gradient induced by the sidewall cooling led to asymmetric descending and ascending flows and irregular LSC. Flow statistics departed from the canonical case, exhibiting lower buoyancy effects, represented by an effective Rayleigh number with effective height dependent on the distance from the lateral cooling. Velocity spectra show two scalings, $\Phi \propto f^{-5/3}$ Kolmogorov (KO41) and $\Phi \propto f^{-11/5}$ Bolgiano (BO59) in the larger Ra; the latter was not present in the smaller set-up. The BO59 scaling with sidewall cooling appears at higher frequencies than its canonical counterpart, suggesting weaker buoyancy effects. The LSC core motions allowed us to identify a characteristic time scale of the order of vortex turnover time associated with distinct vortex modes. The velocity spectra of the vortex core oscillation along its principal axis showed a scaling of $\Phi_c \propto f^{-5/3}$ for the single sidewall cooling, which was dominant closer there. It did not occur in the canonical case, evidencing the modulation of LSC oscillation on the flow.

Key words: Bénard convection

† Email address for correspondence: lpchamo@illinois.edu

1. Introduction

Natural convection induced by heating a fluid body from below and cooling it at the top, so-called Rayleigh–Bénard (RB), has been the subject of intense investigation over a long time due to its scientific and practical relevance in various engineering processes and natural phenomena. Rayleigh number, $Ra = g\alpha\Delta TH^3/\kappa\nu$, Prandtl number, $Pr = \nu/\kappa$, the aspect ratio of the enclosure, $\Gamma = L/H$ and boundary conditions are central parameters characterizing bulk features, which directly influence heat transport in RB convection (Chen & Lavine 1996; Yu, Chang & Lin 1996, 1997; Bailon-Cuba, Emran & Schumacher 2010; Wagner & Shishkina 2013; Stevens, Lohse & Verzicco 2014); here, g is the gravitational acceleration, α is the thermal expansion coefficient, ΔT is the temperature difference between the bottom and top walls, κ is the thermal diffusivity, ν is the fluid kinematic viscosity and L and H are the lengths and the height in a rectangular enclosure, respectively.

At sufficiently high Ra, the flow is dominated by turbulence. It exhibits rich multiscale dynamics with a persistent tendency to organize into a dominant convection roll broadly, usually referred to as a large-scale circulation (LSC), at least for sufficiently small aspect ratios ($\Gamma \sim 1$) (Krishnamurti & Howard 1981; Qiu & Tong 2001*a*; Xia, Sun & Zhou 2003; Xi, Lam & Xia 2004; Zhang *et al.* 2017; Ji & Brown 2020). In such a turbulent RB system, a coherent LSC coexists with bursts of thermal plumes from thermal boundary layers, which modulates the flow statistics (Castaing *et al.* 1989; Wu *et al.* 1990). For example, bulk velocity fluctuations are larger with unstable LSC and extended thermal plumes, whereas they are comparatively smaller with stable LSC and concentrated thermal plumes near the cell edge (Xia *et al.* 2003; Zhang *et al.* 2017). The competition between these two features sometimes results in a flow reversal, which has been observed in many studies. Sugiyama *et al.* (2010) experimentally and numerically analysed LSC reversal in a quasi-two-dimensional square geometry and observed growing corner rolls that take the energy from detaching plumes from the boundary layers. Podvin & Sergent (2012) used proper orthogonal decomposition (POD) to their direct numerical simulation and noted a growth of corner flow during the flow reversal process in a two-dimensional square RB cell. The interaction between small- and large-scale flow also makes complicated mechanisms that drive turbulent energy cascade at different length scales. Bolgiano (1959) and Obukhov (1959) first suggested a scaling for stably stratified convection. For large length scales, namely those above the Bolgiano length, l_B, they assumed that the buoyancy force is more dominant than the inertia and proposed that the mean thermal dissipation rate and the production of thermal expansion coefficient and gravity are relevant parameters to the cascade of turbulent energy in the inertial subrange. The dimensional analysis considering these parameters resulted in a so-called BO59 scaling $E_u(k) \sim k^{-11/5}$ for the energy spectrum. The Bolgiano length is defined as $l_B = (Nu^{1/2}d)/(Pr\,Ra)$, where Nu is Nusselt number and d is the vertical height of the container. Below l_B, inertia becomes more dominant, and one has Kolmogorov–Obukhov scaling (KO41) with a power-law $k^{-5/3}$ for the energy spectrum. See also Bodenschatz, Pesch & Ahlers (2000) for RB convection developments.

The temperature distribution modulates the dynamics of LSC and the statistical properties of thermal plumes in RB convection. Associated effects can be achieved by the sidewall thermal boundary conditions. Verzicco (2002) numerically studied the effects of sidewall with different thermal conductivity on turbulent RB convection for $Ra = 2 \times 10^6 \sim 2 \times 10^9$ and $Pr = 0.7$. They found that the fluid takes additional momentum due to a vertical thermal layer generated by the modified temperature

distribution of the sidewall, which causes mean flow alteration. Zhang *et al.* (2021) numerically and experimentally showed that flow reversal and vertical heat transfer could be controlled by adjusting the configurations with locally isothermal sidewalls in two-dimensional and quasi-two-dimensional RB convection at $Ra \sim 10^8$ and $Pr = 2$ and 5.7. With modulated temperature field near locally isothermal sidewalls, corner rolls against large-scale motions can be restrained or strengthened, affecting flow reversal and heat transfer. Wan *et al.* (2019) studied the effect of sidewall using experiments and direct numerical simulation for a cylindrical RB cell at $Ra = 2 \times 10^5 \sim 4 \times 10^{10}$ and $Pr \sim 0.7$. They noted a strong thermodynamic coupling between the sidewall and fluid that can significantly influence the flow structure and heat transport.

Despite significant progress from previous studies, the effects of asymmetric thermal sidewall boundary conditions in turbulent RB remain obscure. Here, we experimentally investigate features of the LSC and statistics of turbulent fluctuations in RB convection with an asymmetric lateral thermal condition, specifically, one sidewall cooling, and compared with a similar counterpart with adiabatic walls at two reference $Ra = 1.6 \times 10^{10}$ and 2×10^9, and $Pr = 5.4$ to aid insight. This study provides a first experimental inspection of the problem and a basic understanding of natural convection in related asymmetric conditions.

2. Experimental set-up

Laboratory experiments were carried out at two scales in two customized convection tanks (Kim *et al.* 2018, 2020) with the addition of an asymmetric sidewall cooling, one of them having double dimensions. Complementary experiments for each case were also performed in standard RB conditions with adiabatic walls, which served as reference.

The base rectangular tank has adiabatic vertical walls made of double-pane insulated-evacuated glass panels. Each panel is 3.2 mm thick and separated by a 9.5 mm inert gas barrier to minimize heat loss. The side glass walls are sealed using high-temperature RTV (room-temperature-vulcanizing) silicone. The bottom wall of the tank is made of an 11 mm-thick, hydrodynamically smooth aluminium plate. An 800 W flat silicon heater attached to the underside of the plate with a high-temperature silicone adhesive is operated with a temperature controller, which is set to maintain the heating plate at 35 °C. The backside of the heating structure is lined with a pyramidal patterned silicone matt layer that offers an encapsulated air barrier for insulation. A 63.5 mm-thick layer of fire foam was added under the matt coating. A temperature sensor was placed in contact with the underside of the heater and embedded within the foam. A 9.5 mm-thick aluminium plate serves as the seating surface of the underside of the tank. The tank is finished in a solid oak trim secured with fiberglass mesh impregnated with high-temperature silicone; see Kim *et al.* (2018, 2020) for additional details of the tank. Two customized L-shaped, 25 mm-thick aluminium plates were fabricated to provide cooling at the top and one sidewall. A cooling flow was recirculated on these plates by a 1000 W capacity PolyScience refrigerated circulator. It allowed us to keep the temperature of the cooling plates constant, which was set at 25 °C using continuous feedback control. During the experiments, the temperature of heated and cooled plates was monitored using thermocouples (DT4208SD, General Tools & Instruments) at 1 Hz with a measurement resolution of 0.1 °C, and the variation in the temperature of the plates was within 0.2 °C.

The large prismatic tank is $H = 400$ mm high, $B = 500$ mm wide and $L = 250$ mm long and was filled with distilled water. The other set-up is half the size of the large unit. The aspect ratio of the two tanks was $\Gamma = 1.25$, defined by the width per height, or $\Gamma = 0.625$ considering the depth to height ratio. The Prandtl number was $Pr \approx 5.4$ and the reference Ra defined with the temperature difference between bottom and top plates was $Ra = 1.6 \times 10^{10}$ and $Ra = 2 \times 10^{9}$ for the large and small tanks. Overall, the boundary conditions are given by three adiabatic sidewalls and isothermal conditions $T_H = 35\,^{\circ}\mathrm{C}$ at the bottom wall, and $T_C = 25\,^{\circ}\mathrm{C}$ at the top and one sidewall in the asymmetric single sidewall temperature scenario.

Flow measurements were obtained in various planes in two distinct sets, one of a relatively short duration of approximately 360 s per plane at 10 Hz to characterize critical motions, henceforth Group 1. The other set, referred to as Group 2, considered comparatively long runs of 6000 s at lower frequency sampling of 0.67 Hz to obtain representative statistics. Instantaneous flow fields in Group 1 were captured at five vertical planes perpendicular and parallel to the cooling sidewall using particle image velocimetry (PIV). Specifically, in-plane flow was obtained in three y–z parallel planes at $x/B = 1/4$, 1/2 and 3/4 covering a FOV of 250 mm × 400 mm (see figure 1*a*), and two x–z parallel planes at $y/L = 1/3$ and 2/3 covering an investigation area of 500 mm × 400 mm (see figure 1*b*). A 4-MP CMOS high-speed camera was used to capture the flow in the y–z planes and two cameras for the x–z planes, which shared an overlap region of 100 mm × 400 mm in the middle of FOV. Before each experiment, the system was allowed to reach steady conditions by waiting for at least 30 minutes; it minimized the transient effects on the flow. The FOVs were illuminated with an 80 W, 532 nm high-speed laser during the investigation. There were 4000 and 3000 instantaneous fields obtained in each of y–z and x–z FOVs, all at a sampling rate of 10 Hz. For PIV processing, two-dimensional velocity fields were obtained from cross-correlation between two consecutive images with a time interval of 100 ms. Each velocity vector was calculated in a subwindow of 60 pixels × 60 pixels with 50 % overlap resulting in approximately 4 mm vector grid spatial resolution. The complementary experiments on the smaller rectangular tank considered experimental conditions identical to those in Group 2. The smaller set-up had a FOV of 250 mm × 200 mm, which allowed a higher grid resolution of $\Delta x = \Delta y = 1$ mm.

Long-duration experiments in Group 2 considered flow characterization for 100 minutes to explore statistical quantities and the LSC motion. The PIV with an 8 MP CCD camera and a 250 mJ, 532 nm low-speed laser was performed at a sampling frequency of 0.67 Hz in two vertical parallel planes $y/L = 1/3$ and 2/3. The vector grid resolution and investigation area in Group 2 was same as that in Group 1. Flow field characterization was also obtained at one vertical parallel plane $y/L = 1/2$ for the base case without single sidewall cooling. A 100 mm-thick insulation board with a thermal conductivity similar to the other side air-gap walls replaced the sidewall cooling. This set-up produced a typical RB convection domain with a geometry the same as the single sidewall cooling case. Here, the heating and cooling plate temperatures were also maintained at 35 °C and 25 °C, the same as the single sidewall cooling case. Interestingly, a reversal of LSC appeared after a relatively long time for this case without single sidewall cooling. This phenomenon is discussed later. An additional long-duration experiment was conducted at $y/L = 1/2$ and $y/L = 1/3$ planes, avoiding flow reversal to obtain time-averaged statistics. This was possible by slightly tilting the convection cell with a slight angle $\sim 1^{\circ}$ as suggested by Qiu *et al.* (2004) and Ciliberto, Cioni & Laroche (1996).

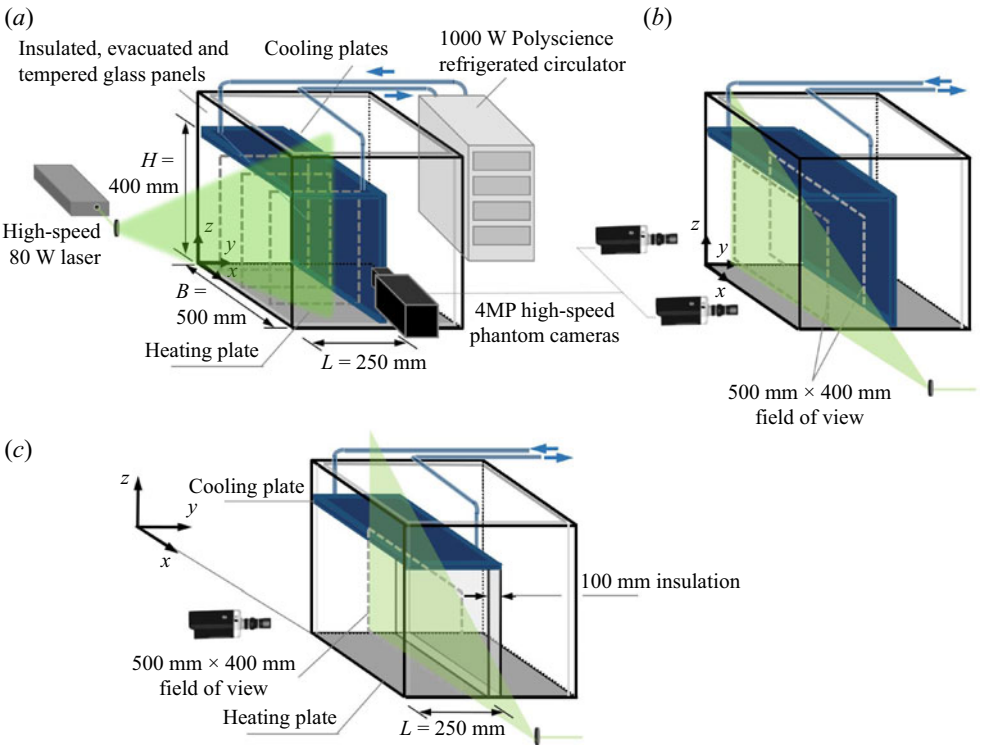

Figure 1. Basic schematic of the experimental set-ups with the large tank illustrating the case with single sidewall cooling with (*a*) three field of views (FOVs) in the y–z planes at x/B = 1/4, 1/2 and 3/4 and (*b*) two FOVs in the x–z planes at y/L = 1/3 and 2/3. (*c*) Standard RB configuration (no sidewall cooling) showing an x–z FOV plane at $y/L = 1/2$. A similar set-up was studied with a smaller tank of half the size; see Appendix A.

3. Results

3.1. *Time-averaged flow field statistics*

3.1.1. *On the mean flow*

Characterizing the mean flow field using experiments in Group 1 provides a first assessment of the LSC signature. Unless specified otherwise, the discussion is centred at larger Ra and complemented at lower Ra when appropriate and in Appendix A. The velocities are normalized by a freefall velocity $V_f = \sqrt{\alpha g \Delta T H}$. It demonstrates the modulation of the asymmetric single sidewall cooling on the circulation pattern. In particular, the distribution of the vertical velocity component, W, shown in figure 2, highlights a dominant LSC pattern and local and non-local effects due to single sidewall cooling. A comparable downward and upward flow region in spatial extent and velocity level occurs in the parallel plane far from the cooling wall, i.e. $y/L = 1/3$. However, this is not the case at the plane closer to the cooling sidewall, $y/L = 2/3$; the spatial distribution and relative magnitude of the maximum vertical velocity differ significantly with locally stronger descending bulk flow. The downward motion particularly dominates near the side cooling wall. The W distribution in all y–z planes indicates the effect of the induced density gradient with a denser medium in the proximity to the vertical cooling wall. As a result, the ascending and descending flows of the LSC undergo spatial changes. It is also worth highlighting the match between the intersected planes, which gives qualitative

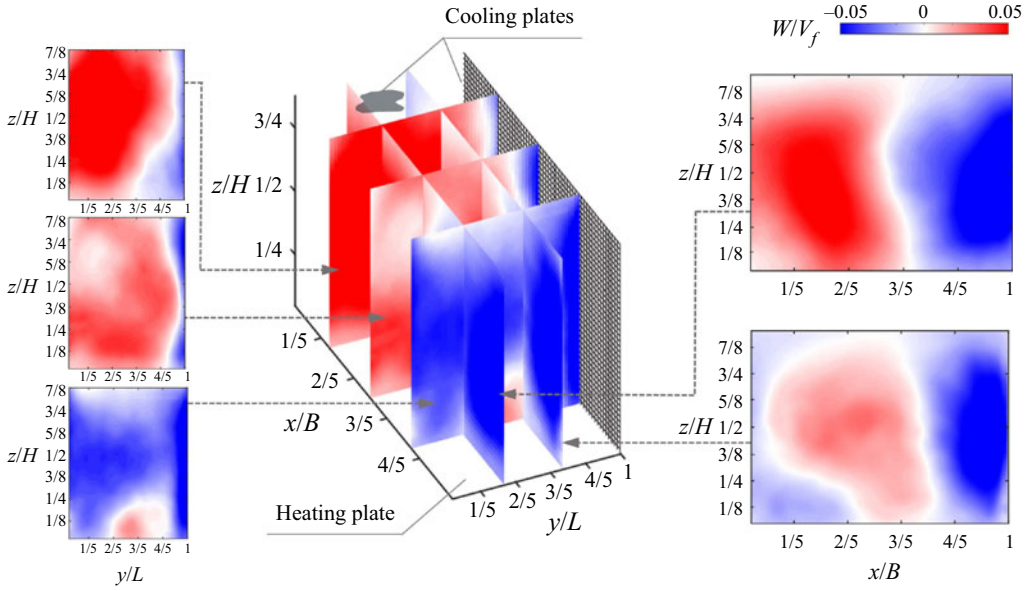

Figure 2. Time-averaged vertical velocity component, W, at various x–z and y–z planes for the Group 1 measurements.

evidence of the repeatability of the process. Indeed, given the large domain in each plane, flow characterization in the normal planes was obtained separately. Overall, the planes show an LSC with a significant bulk sense of rotation pointing in the y axis induced by the thermal gradient from the top and bottom walls. The single sidewall cooling directly caused a secondary rotating pattern in the x axis. Note that for a conventional RB in a rectangular geometry, the LSC is expected to rotate pointing to the shorter horizontal dimension (Huang, Hu & Li 2019), which is parallel to the y axis in this case. Inspection of these axes of rotation allows for characterizing the bulk motions of the LSC, which will be given in the last section.

The distributions of the mean horizontal velocity components, U and V, parallel to the x and y axes, illustrated in figure 3 help us to appreciate the two senses of rotation with respect to the defined coordinate system; those are projections of an overall inclined rotation pattern of the dominant LSC. The non-symmetrical distributions of the horizontal velocity components in each plane are conditioned by the vertical counterpart given in figure 2. Note that the magnitude of the y axis rotation motion, i.e. mean velocity in the x–z planes, is larger than that of the x axis rotation motion, i.e. mean velocity in the y–z planes. This supports the observation of the relative modulation of the top and bottom cold-and-hot walls in the first case and side cold-and-adiabatic walls in the second case.

Out of plane bulk vorticity fields, ζ_y and ζ_x, superimposed with the mean in-plane velocity vector fields shown in figure 4, provide additional insight into the bulk recirculation patterns of the LSC and secondary structures. A roughly centred rotation pattern covers a significant fraction of the cell domain relatively far from the side cooling wall ($y/L = 1/3$, figure 4*a*). However, the LSC shows a highly asymmetric shape with local counter-rotating regions closer to the sidewall cooling ($y/L = 2/3$, figure 4*b*). These counter-rotating regions appear in standard RB at smaller Ra (Sugiyama *et al.* 2010; Zhang *et al.* 2017). The characteristic of corner flow is also demonstrated in the x–z planes, where comparatively small structures occur at the top and bottom corners in proximity

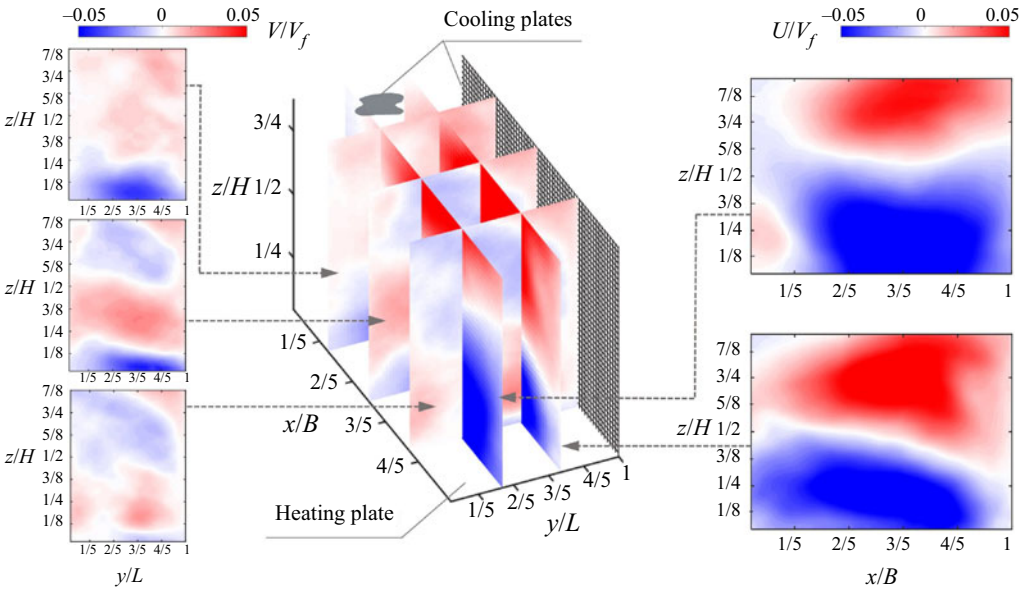

Figure 3. Time-averaged horizontal velocity components, U and V in the x and y directions for the Group 1 measurements. Note that these components are normal; they should not match at the plane intersections.

to the cooling wall. This phenomenon evidences the effect of sidewall cooling by inducing an effective Rayleigh number (Ra_e) and a preferential buoyancy gradient that breaks the symmetry of LSC. The identical trends are also observed in the long-duration experiment shown in figure 5. For brevity, we present results in the representative midplane, $y/L = 1/2$, for the canonical RB case; see figure 14 in Appendix A for the comparison with the $y/L = 1/3$ plane. The mean flow configuration at $Ra = 2 \times 10^9$ also revealed similar bulk effects of lateral cooling; see figure 15 in Appendix A. Detailed discussion and further arguments relating to a Ra_e and interaction between LSC and small-scale coherent structures are given in later sections.

3.1.2. *Second-order flow statistics*

In-plane turbulent kinetic energy $TKE = 1/2(\langle u'^2 \rangle + \langle w'^2 \rangle)$ and kinematic Reynolds shear stress $-\langle u'w' \rangle$ are obtained from the long-duration experiments (Group 2) in two planes parallel to the vertical cooling (x–z) and compared with a canonical RB convection scenario in figure 6. There, $u'(t) = u(t) - U$ and $w'(t) = w(t) - W$ are the velocity fluctuations in the x and z directions and $\langle\ \rangle$ represents the time-average operator.

The TKE and Reynolds stress distribution in the canonical RB convection case (no single sidewall cooling) is consistent with those observed in the literature for similar Ra and Pr numbers (Xia *et al.* 2003; Zhang *et al.* 2017), exhibiting similar levels of normalized Reynolds stress to those in Xia *et al.* (2003). However, the distribution of this quantity in the asymmetric cooling is significantly different; it results from a combined effect on Ra_e and the preferential density gradient breaking up the symmetry of the LSC.

In canonical RB convection, Ra is defined as the ratio between time scales of thermal transport by buoyancy and convection effects (Rayleigh 1916) and is proportional to the H^3, where H is the separation between the lower and upper boundaries having temperatures $T + \Delta T$ and T (figure 7*a*). However, the single-sidewall cooling scenario

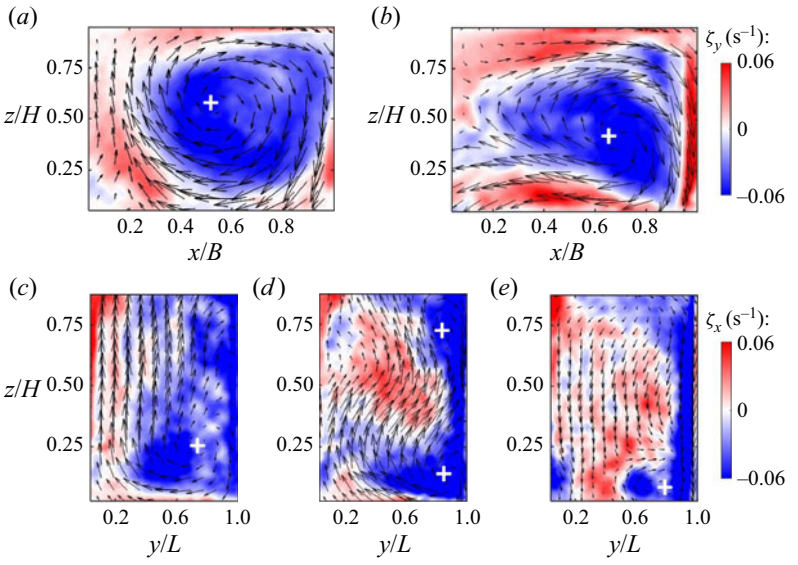

Figure 4. Out-of-plane bulk vorticity contours superimposed with in-plane mean velocity vector distributions in the x–z planes at y/L = (*a*) 1/3 and (*b*) 2/3, and y–z planes at x/B = (*c*) 1/4, (*d*) 1/2 and (*e*) 3/4. The '+' signs indicate the location of mean vortex cores.

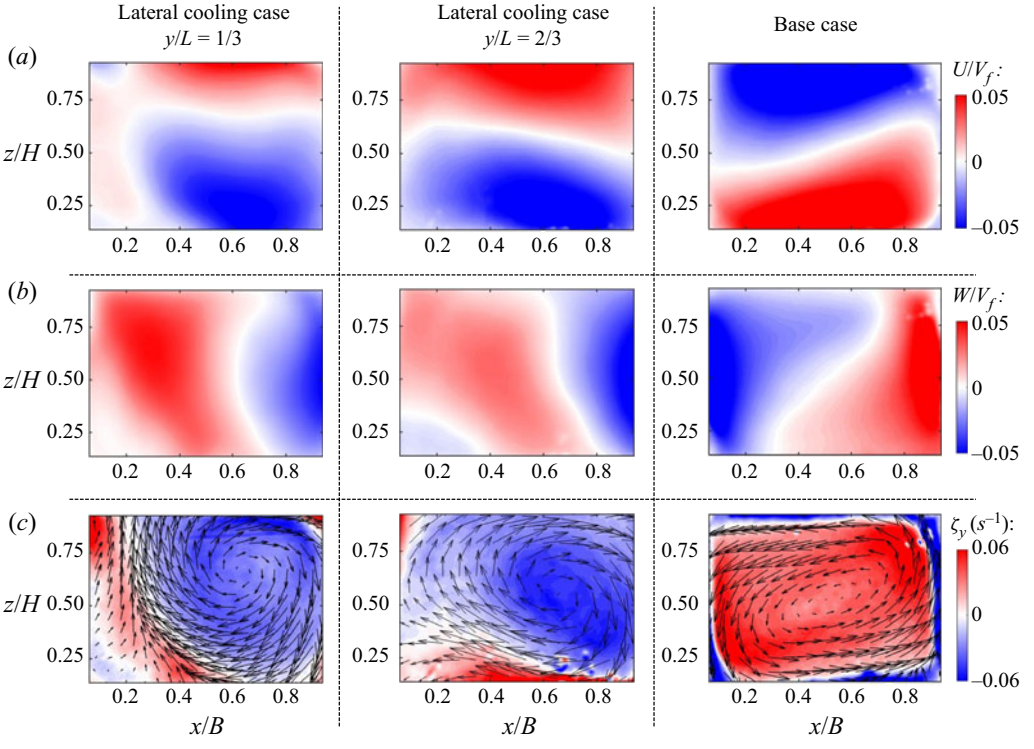

Figure 5. Time-averaged (*a*) horizontal and (*b*) vertical velocity fields, and (*c*) vorticity contours with superimposed in-plane velocity vector fields for Group 2 measurements.

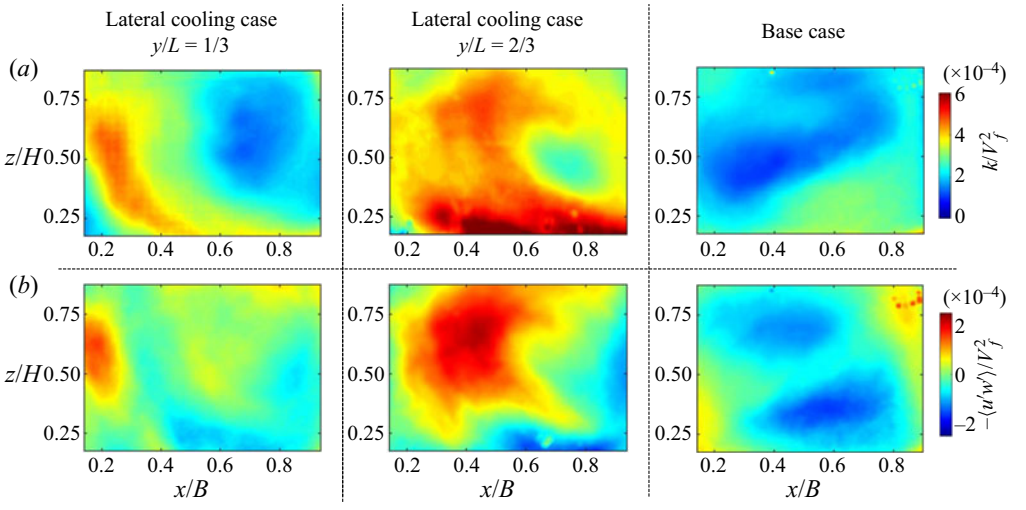

Figure 6. In-plane (*a*) turbulent kinetic energy and (*b*) Reynolds stress for Group 2 measurements.

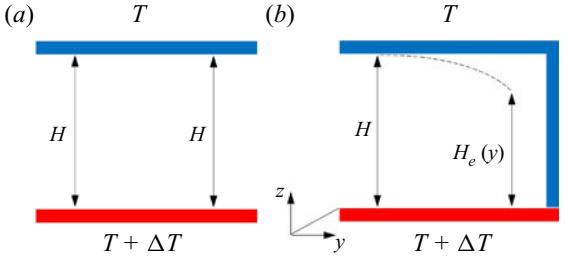

Figure 7. Conceptual schematic of the *y*-dependent H_e due to the modulation of the lateral cooling. (*a*) Canonical RB convection, and (*b*) RB convection with single sidewall cooling.

modifies the distance from the cooling; its magnitude is *y*-dependent (figure 7*b*). As such, we propose an effective length scale $H_e(y)$ that should weigh the relative cooling sidewall, as shown in figure 7(*b*). This quantity may better capture the buoyancy time scale. Although further investigation is required to obtain an accurate estimator of $H_e(y)$, results indicate that this quantity increases with the distance from the lateral cooling such that $H_e(y) \to H$ sufficiently far from it, where sidewall effects become negligible. Indeed, compared with their canonical counterpart, a relatively lower Ra_e signature is indicative at the $y/L = 2/3$ plane. Consequently, an effective Rayleigh number may be expressed as $Ra_e = g\alpha\Delta T H_e^3/\kappa\nu$.

Second-order statistics provide evidence of the Ra_e effect, which modulates temperature distribution. In the canonical scenario, a comparatively high *TKE* region tends to concentrate around the external portion of the cell. In the lateral cooling case, a relatively high *TKE* region extends over the cell centre, implying that the thermal plumes extend farther than the canonical case. This trend is more distinct in the plane closer to the cooling wall ($y/L = 2/3$), indicating a lower Ra_e, whereas in the plane farther apart from lateral cooling ($y/L = 1/3$) shows relatively higher Ra_e. Canonical RB at the higher *Ra* of 1.6×10^{10}, the detaching thermal plumes from the thermal boundary layers are restricted to the thin boundary layer as the vertical temperature gradient is mainly in the near-wall region (Xia *et al.* 2003; Wagner & Shishkina 2013) leading to the high *TKE* corners.

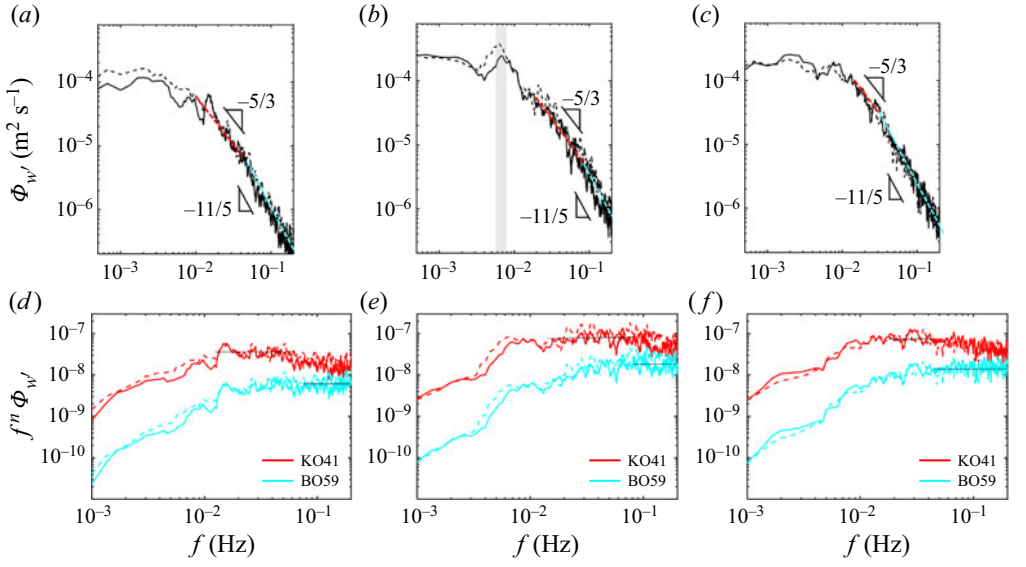

Figure 8. (*a–c*) Power spectra of vertical velocity fluctuations, $\Phi_{w'}$, (*d–f*) compensated forms $f^{5/3}\Phi_{w'}$ (KO41) and $f^{11/5}\Phi_{w'}$ (BO59) at the vortex core location (solid line) and at $\Delta x/B = 0.2$ from the vortex core in the horizontal direction (dashed line) for the single sidewall cooling case at (*a*,*d*) $y/L = 1/3$ and (*b*,*e*) $y/L = 2/3$. (*c*,*f*) Canonical counterpart (no sidewall cooling).

The PIV measurements in the midplane region of this canonical RB did not include that zone, but it was captured with complementary experiments at the $y/L = 1/3$ plane and illustrates a high *TKE* region at the right-hand top corner (Appendix A, figure 14*d*). However, lateral cooling altered the temperature distribution leading to a non-zero temperature gradient featuring trends reported by Wang *et al.* (2021) for a pure lateral-heating scenario. In our lateral cooling case, the temperature gradients are less restricted to the near-wall region than the canonical RB convection resulting in a high *TKE* region around the centre. Higher *TKE* region towards the centre of the flow field for a lower *Ra* is consistent with those reported for canonical RB convection (Xia *et al.* 2003; Zhang *et al.* 2017). Aside from altering the *Ra*, an additional asymmetry effect due to the preferential negative buoyancy force generated from sidewall cooling is evidenced by comparing the base case's *TKE* distribution with the single sidewall cooling case. A similar effect is observed from the $-\langle u'w'\rangle$ distributions, as shown in figure 6(*b*). Second-order flow statistics in the smaller set-up at $Ra = 2 \times 10^9$ also showed similar effects of single sidewall cooling, but the effects were less dependent on the distance from the sidewall cooling compared with the case at $Ra = 1.6 \times 10^{10}$; see Appendix A, figure 16.

3.2. *Spectral features of the flow*

Using the long-time experimental data in Group 2, we explored the impact of the single sidewall cooling on the structural features of the turbulence at selected locations. Figure 8 illustrates power spectra of the vertical velocity fluctuations, $\Phi_{w'}$ and their compensated forms, at two points in each plane parallel to the sidewall cooling, one at the vortex core (solid line) and the other at $\Delta x/B = 0.2$ from the vortex core in the positive horizontal direction (dashed line), where the shear is significant.

The velocity spectra exhibit a similar trend at two locations in a given plane and scenario, where similar spectral features are observed within the flow field. However, they reveal different scaling ranges depending on the presence of the single sidewall cooling and the distance from that wall. The two scenarios exhibit a $\Phi_{w'} \propto f^{-5/3}$ (KO41) scaling in the comparatively low-frequency range within the inertial subrange and a $\Phi_{w'} \propto f^{-11/5}$ (BO59) law at a sufficiently high frequency. The frequency defining the start of the BO59 scaling is the highest for the plane near the cooling sidewall (~ 0.09 Hz, figure 8*b*) and lower at the $y/L = 1/3$ plane (~ 0.06 Hz, figure 8*a*), and is lowest in the canonical base case (~ 0.05 Hz, figure 8*c*) evidencing the dominant effect of the sidewall cooling in the near flow dynamics.

Considering that KO41 and BO59 scalings feature inertia and buoyancy effects, the results suggest weaker buoyancy effects, i.e. lower Ra_e, due to the modulated temperature distribution with the sidewall cooling. The inertia- and buoyancy-driven ranges are expected to occur at comparatively small and large length scales (Bolgiano 1959; Obukhov 1959). However, a similar trend in frequency power spectrum for the vertical velocity was noted by Shang & Xia (2001); power laws of -1.35 and $-11/5$ at comparatively low- and high-frequency ranges. They also pointed out an inconsistency between the theoretical studies and their findings, stressing the necessity for further investigation. The complex interaction between small- and large-scale structures with small-scale thermal plumes organizing to form a large-scale flow that progresses to small scales (Xi *et al.* 2004; Zhang *et al.* 2017) is a factor that can shed light on this particular dynamics.

It is worth pointing out that the standard deviations of the vertical velocity component, σ_w, is the largest at the plane closer to the cooling wall. A distinct low-frequency peak highlighted in figure 8(*b*) is a particular feature of turbulent convection; it is of the order of the turnover frequency for the LSC, $f_t = \langle \sigma_w \rangle / 2H$ (Qiu & Tong 2001*b*; Sakievich, Peet & Adrian 2016). This turnover frequency is approximately 3.9×10^{-3} Hz for the single sidewall cooling case. The peak frequency in figure 8(*b*) is approximately $2f_t$, matching the canonical RB convection studies with two LSC oscillation periods per LSC turnover time (Brown & Ahlers 2009; Ji & Brown 2020). The structural features at $Ra = 2 \times 10^9$ are presented in figure 17 in Appendix A, showing only KO41 scaling and peak frequencies that match LSC turnover time. A detailed discussion of the LSC oscillation is given in § 3.4.

3.3. *Proper orthogonal decomposition*

Distinct spatial features produced in the given flows, including dominant coherent motions, can be further evidenced with snapshot POD (Sirovich 1987). This technique is a valuable tool to uncover flow characteristics affected by coherent structures (Rempfer & Fasel 1994). Recently, Paolillo *et al.* (2021) showed that POD modes may extract characteristic LSC within the RB turbulent thermal convection process, and the mode coefficients allow the determination of LSC orientation.

The POD basically decomposes the stochastic velocity $\boldsymbol{u}(x, y, t)$ into deterministic spatially correlated patterns $\phi^n(x, y)$ as POD modes and their time-dependent coefficients, $a^n(t)$, as follows:

$$\boldsymbol{u}(x, y, t) = \sum_{n=1}^{N} a^n(t)\phi^n(x, y). \tag{3.1}$$

Here, $N = 4000$ is the number of snapshots. The energy content, E_n, is obtained by dividing the eigenvalue of a particular mode by the sum of all N eigenvalues (Hamed *et al.* 2017), i.e. $E_n = \lambda_n / \sum_{m=1}^{N} \lambda_m$, and can be interpreted as the single-mode contribution to

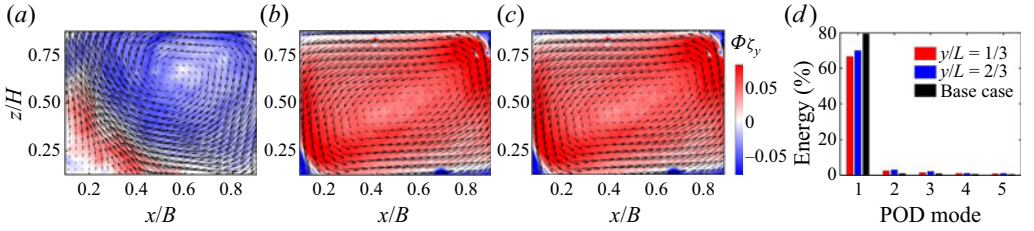

Figure 9. Vorticity contours of the sum of first two POD modes superimposed with velocity vector fields in (*a*) $y/L = 1/3$ and (*b*) $y/L = 2/3$ planes for single sidewall cooling case, and (*c*) for the base case. (*d*) Energy of the first five modes.

the total kinetic energy. The first mode corresponds to the mean flow, shown in figure 5, and displays an LSC with comparatively small counter-rotating regions and the first two modes contribute to almost 70 % of the total kinetic energy (figure 9*d*); a simple low-order model may consider the first two modes as $\boldsymbol{U} = \sum_{i=1}^{2} a^i \boldsymbol{\phi}^i$, where $\boldsymbol{U} = [\boldsymbol{uv}]^\intercal$ is the reduced velocity vector. Figure 9(*a*,*b*) demonstrate the out-of-plane vorticity ζ_y of the low-order model with velocity vectors. It shows a large rotating flow with the same direction as the LSC given in the first mode, but counter-rotating regions become more prominent in the two planes parallel to the sidewall cooling and reveal that the counter-rotating flow is larger in the plane of lower Ra_e closer to the vertical cooling wall, and agrees well with the larger counter-rotating flow at lower Ra for canonical RB convection. Xia *et al.* (2003) noted that counter-rotating vortices are related to the regions where the vertical velocity fluctuations are large, where rising and falling plumes may reach the opposite wall. As indicated in § 3.1.2, large velocity fluctuation regions are more extended in the $y/L = 2/3$ plane, implying that thermal plumes advect farther and generate larger counter-rotating flows with the single sidewall cooling. An additional difference between the LSC and counter-rotating flows for the single sidewall cooling case and canonical RB convection is the asymmetry of the coherent structures. Counter-rotating flows are located symmetrically for the canonical RB scenario where LSC's ascending and descending motions decelerate at the corners (figure 9*c*). However, with sidewall cooling, counter-rotating regions are mostly leaned towards the bottom side (figure 9*a*,*b*) as the result of additional cooling, which restrains the deceleration of descending motion of LSC. Thus, suppressing the generation of corner flows at the top corner, resulting in an asymmetric flow configuration.

It is worth pointing out a flow reversal in the base case as indicated by the first POD mode coefficient in figure 10(*b*). Instantaneous vector fields before flow reversal, during the change of rotation, and after the reversal are shown in figure 11. The flow reversal was suppressed with a minor tilting, which is evidenced by the constant sign of the first mode coefficient (figure 10*c*). Similarly, flow reversal was suppressed in the single sidewall cooling case. The asymmetric flow configuration prevented the flow reversal even under significant counter-rotating flow. Huang *et al.* (2015) pointed out that more reversals are required with a symmetric boundary condition to restore the symmetry, and controlling the flow reversal with an asymmetric thermal boundary condition was also proved in Zhang *et al.* (2021). Single sidewall cooling can also lead to a symmetry-breaking process similar to the base case with tilting. Note that a minor tank tilting in the base case generates a buoyancy force component in the tilted direction, which directly induces a preferential orientation of the LSC rotation. Small perturbations may modulate the direction of LSC in canonical RB convection; however, the asymmetric vertical cooling pins down the LSC direction by creating a density gradient in the y direction. Due to this, descending flow

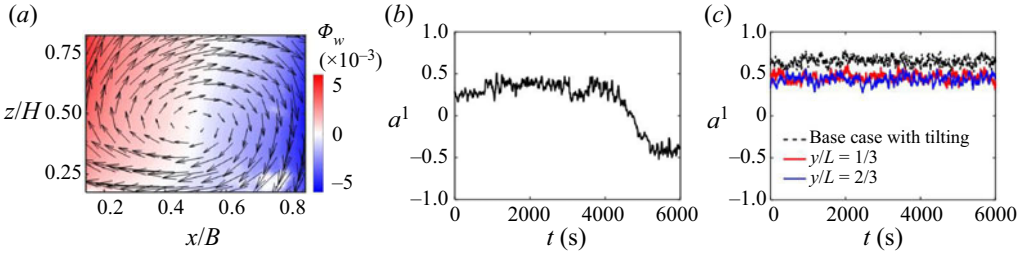

Figure 10. Vertical velocity snapshot of (*a*) first POD mode superimposed with velocity vector fields and (*b*) associated mode coefficient for the base case without tilting. (*c*) First mode coefficients for the base case with tilting and single sidewall cooling case.

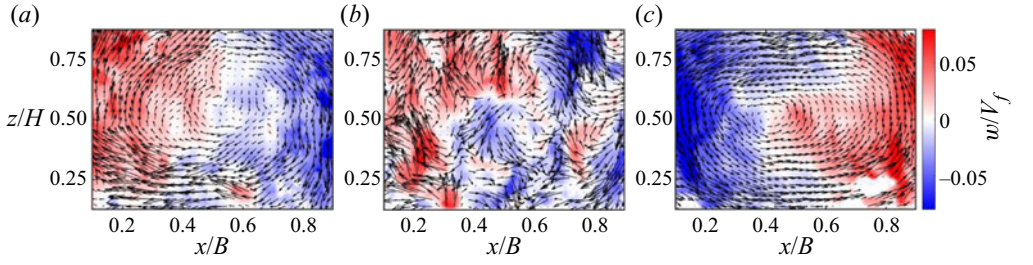

Figure 11. Instantaneous vector fields with vertical velocity contours at an instant (*a*) before, (*b*) during and (*c*) after the flow reversal for the base case without tilting.

is stronger and more tilted to one side of the x direction by mass conservation closer to the cooling sidewall ($y/L = 2/3$) compared with that at the $y/L = 1/3$ plane, as shown in figure 2. As the heavier fluid ($y/L = 2/3$) is more tilted to one side of the x direction than the lighter fluid ($y/L = 1/3$), a density gradient in the x direction is generated in a mediated manner; this promotes the LSC direction. In conclusion, the asymmetric set-up creates a preferential density gradient resulting in a driving force for a particular rotational direction of the LSC.

3.4. *On the LSC oscillation pattern*

Inspection of the LSC core oscillation aids in understanding the impact of the single sidewall cooling on the dominant flow patterns. The LSC's global minimum velocity magnitude defines the vortex core location. The trajectory in each plane is provided in figure 12; the black dot and line represent the time-averaged vortex core location and the principal direction of the oscillating vortex core computed by a principal component analysis (Ringnér 2008). The vortex core oscillates approximately horizontally along the principal axis inclined $< 15^\circ$ with respect to the x axis (figure 12*c*) in the canonical case. However, bulk inclinations of approximately 35° and -40° in the $y/L = 1/3$ and $y/L = 2/3$ planes (figure 12*a*,*b*) with substantial vertical motions occurred with the single sidewall cooling.

The time-averaged inclination angle of the LSC is obtained by connecting the vortex core locations between the two parallel planes (figure 12*d*). From this, angles α and β are defined by intersecting the line connecting two time-averaged vortex core locations with

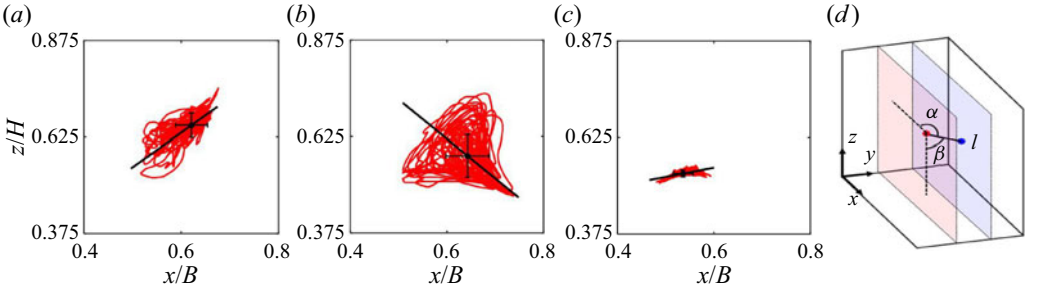

Figure 12. In-plane trajectory of the vortex core for single sidewall cooling case in (*a*) $y/L = 1/3$ and (*b*) $y/L = 2/3$ planes, and for (*c*) base case. The black lines and dots indicate principal directions and time-averaged vortex core locations; standard deviations of horizontal and vertical locations are presented with error bars. (*d*) Schematics of the time-averaged inclination angles of the LSC, α and β. The red and blue dots are the time-averaged vortex core locations in $y/L = 1/3$ and $y/L = 2/3$ planes.

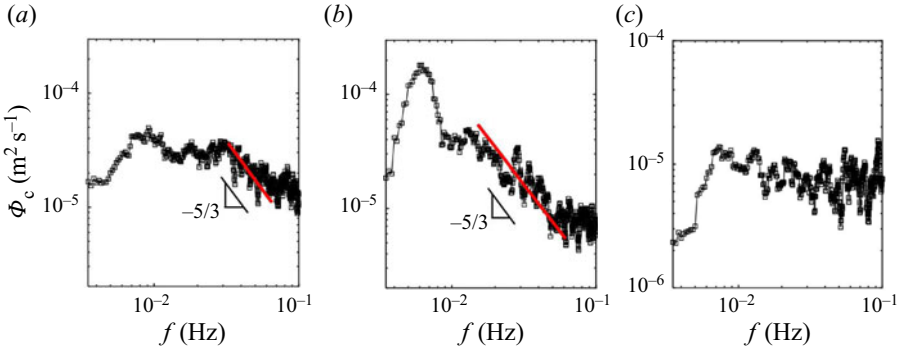

Figure 13. Frequency spectra of the velocity of vortex core oscillations with respect to its principal axis, Φ_c, for the single sidewall cooling case at (*a*) $y/L = 1/3$ and (*b*) $y/L = 2/3$, and (*c*) for the base case.

the x and z axes, i.e.

$$\alpha = \cos^{-1}\left(\frac{\boldsymbol{l}\cdot\boldsymbol{e_x}}{|\boldsymbol{l}|}\right), \quad \beta = \cos^{-1}\left(\frac{\boldsymbol{l}\cdot\boldsymbol{e_z}}{|\boldsymbol{l}|}\right). \tag{3.2a,b}$$

The unit vector $\boldsymbol{l}/|\boldsymbol{l}|$ points in the direction of the vortex core locations between the $y/L = 2/3$ and $y/L = 1/3$ planes, and $\boldsymbol{e_x}$ and $\boldsymbol{e_z}$ are unit vectors in the x and z directions. Here, $\alpha \sim 97^\circ$ and $\beta \sim 69^\circ$, indicating a comparatively large tilting with respect to the z axis and negligible tilting with respect to the x axis. The tilting in z direction shows the effect of single-sided cooling, which pulls down the LSC near the cooling sidewall. Note that $\alpha = \beta = 90^\circ$ under no tilting.

Further insight into the LSC core motions is obtained with the core velocity spectra of the projected in-plane vortex core oscillations in the principal axis, Φ_c, which is shown in figure 13. Note the chaotic-like motion $\Phi_c \propto f^0$ in the base case (figure 13*c*), showing that the base case LSC is essentially not affected by the flow velocity fluctuations, which is mostly driven by buoyancy as shown in figure 8. However, a $\Phi_c \propto f^{-5/3}$ scaling occurs in the single sidewall cooling cases (figure 13*a*,*b*) which is more prominent closer to the sidewall cooling ($y/L = 2/3$, figure 13*b*). This may be attributed to

combining effects of relatively large velocity fluctuation created by the thermal plumes discussed in § 3.1.2 and relatively smaller size of LSC with asymmetric features as indicated in figure 9(*b*) for the plane closer to the cooling wall. Additionally, a dominant peak in Φ_c near the cooling wall is associated with that in the velocity spectra at $y/L = 2/3$ (figure 8*b*). It has a characteristic time scale of the order of the vortex turnover time reminiscing the sloshing, torsional and jump rope vortex LSC modes (Funfschilling, Brown & Ahlers 2008; Zhou *et al.* 2009; Vogt *et al.* 2018; Ji & Brown 2020; Horn, Schmid & Aurnou 2021). It is worth pointing out that this scaling holds for the vortex core fluctuation projected to the minor principal axis, not shown for brevity.

4. Conclusions

Close inspection of the flow at two Rayleigh numbers evidenced a strong modulation of the single sidewall cooling in RB convection on the spatial and temporal features of the LSC and statistics and structure of the flow. In particular, the single-sidewall cooling modulated flow structures in distinct ways. Flow asymmetry was promoted by strong descending motions near the vertical cooling wall, shaping the LSC's spatial features. It also played an essential role in suppressing the flow reversal with a similar effect to tilting the convection cell in a canonical RB scenario. Aside from the asymmetric effects, signatures of lower buoyancy effects may be represented by a lower effective Rayleigh number, $Ra_e = g\alpha\Delta T H_e^3/\kappa\nu$, where H_e is the effective height. The lower Ra_e resulted in changes in the bulk velocity fluctuations and larger corner flows, which were dominant closer to the cooling sidewall. In the larger Ra scenario, velocity spectra indicate two scalings, $\Phi \propto f^{-5/3}$ Kolmogorov (KO41) and $\Phi \propto f^{-11/5}$ Bolgiano (BO59). Compared with the canonical counterpart, the BO59 scaling appears at relatively high frequencies, suggesting weaker buoyancy effects (i.e. lower Ra_e) with lateral cooling. For the smaller Ra, BO59 scaling is not present. Inspection of the LSC core motion patterns reveals significant multiscale oscillations with spectral scaling implying the modulation of the sidewall cooling compared with the canonical counterpart and the strong linkage with the velocity fluctuations across scales. The oscillation of LSC characterized by projections of the vortex core trajectories evidence larger vortex core motions with the sidewall cooling. The velocity spectra of the vortex core oscillation along its principal axis, Φ_c, exhibited a negligible relationship between the velocity fluctuations and the LSC oscillation in the canonical RB scenario with a flat Φ_c. However, a strong relation occurred in the single sidewall cooling case, which was dominant at the plane closer to the sidewall cooling with a $\Phi_c \propto f^{-5/3}$ scaling and a robust spectral peak frequency of the order of the vortex turnover time.

The dynamics of the LSC and dependence on distinct boundary conditions deserve further exploration; the future effort will focus on exploring this using a Lagrangian perspective and the implications on inertial particles.

Funding. This research was funded by the National Science Foundation, grant no. CBET-1912824.

Declaration of interests. The authors report no conflict of interest.

Author ORCIDs.
Shyuan Cheng https://orcid.org/0000-0001-8563-9054;
Leonardo P. Chamorro https://orcid.org/0000-0002-5199-424X.

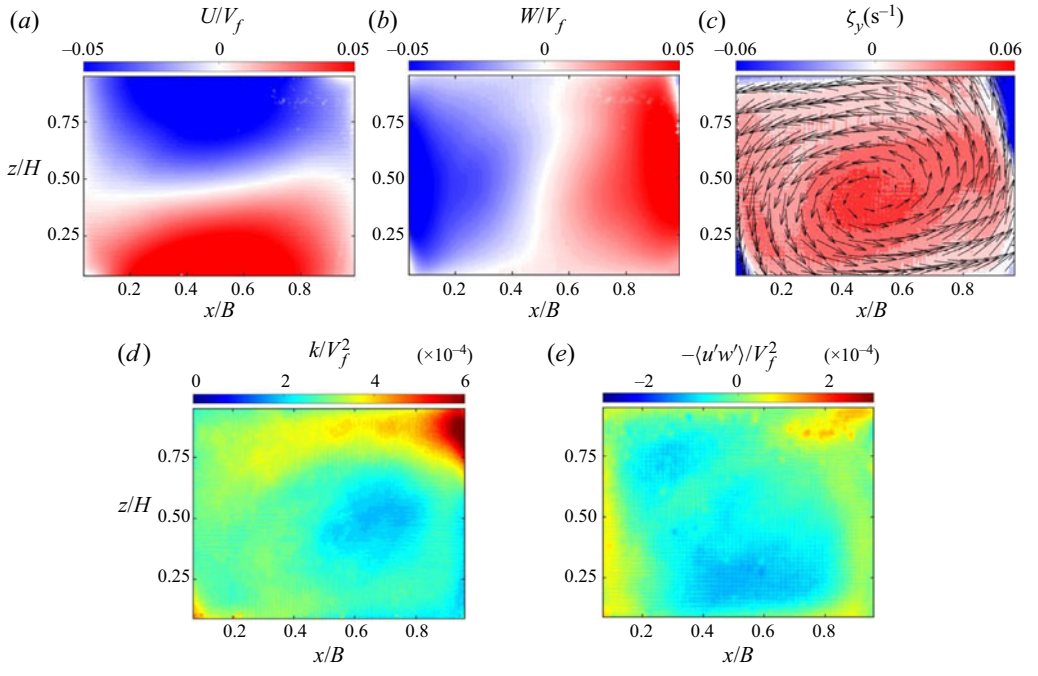

Figure 14. Time-averaged distributions of the (*a*) horizontal and (*b*) vertical velocity fields, (*c*) vorticity contours with superimposed in-plane velocity fields, (*d*) in-plane turbulent kinetic energy, and (*e*) Reynolds stress for the canonical RB case in the $y/L = 1/3$ plane at $Ra = 1.6 \times 10^{10}$.

Appendix A

A.1. *Complementary flow fields in the canonical case at* $Ra = 1.6 \times 10^{10}$

Flow statistics in the canonical RB convection in the $y/L = 1/3$ plane are included in figure 14 for comparison with those at the midplane. The mean flow in the $y/L = 1/3$ plane shows symmetric LSC similar to the results in the midplane (figure 14*a–c*). Distributions of second-order flow statistics are also comparable in two planes (figure 14*d*,*e*). However, we captured high *TKE* region in the $y/L = 1/3$ plane at the right-hand top corner (figure 14*d*) that is missed in the midplane due to the PIV FOV there.

A.2. *Flow features at the lower* $Ra = 2 \times 10^9$

Complementary experiments were conducted with a canonical RB convection and a configuration with single sidewall cooling at $Ra = 2 \times 10^9$ to aid insight. As indicated in § 2, these tests used tanks with half of the dimension of the large set-up, i.e. the smaller rectangular cell has a dimension of $H = 200$ mm, $B = 250$ mm and $L = 125$ mm. The signature of effective Rayleigh number and asymmetry effect discussed for the large scenario applies to the mean flow and the second-order flow statistics at the lower $Ra = 2 \times 10^9$. Also, larger corner flow and tilting structures occurred with sidewall cooling. However, the effects are less dependent on the distance from the sidewall cooling compared with the case with one order of magnitude higher Ra ($= 1.6 \times 10^{10}$). It has similar flow structure (figure 15) and *TKE*, Reynolds stress distributions (figure 16), shown for $y/L = 1/3$ and $y/L = 2/3$ planes. In addition, velocity spectra reveal peak frequency that matches the turnover time in the lateral cooling and the canonical cases with the lower

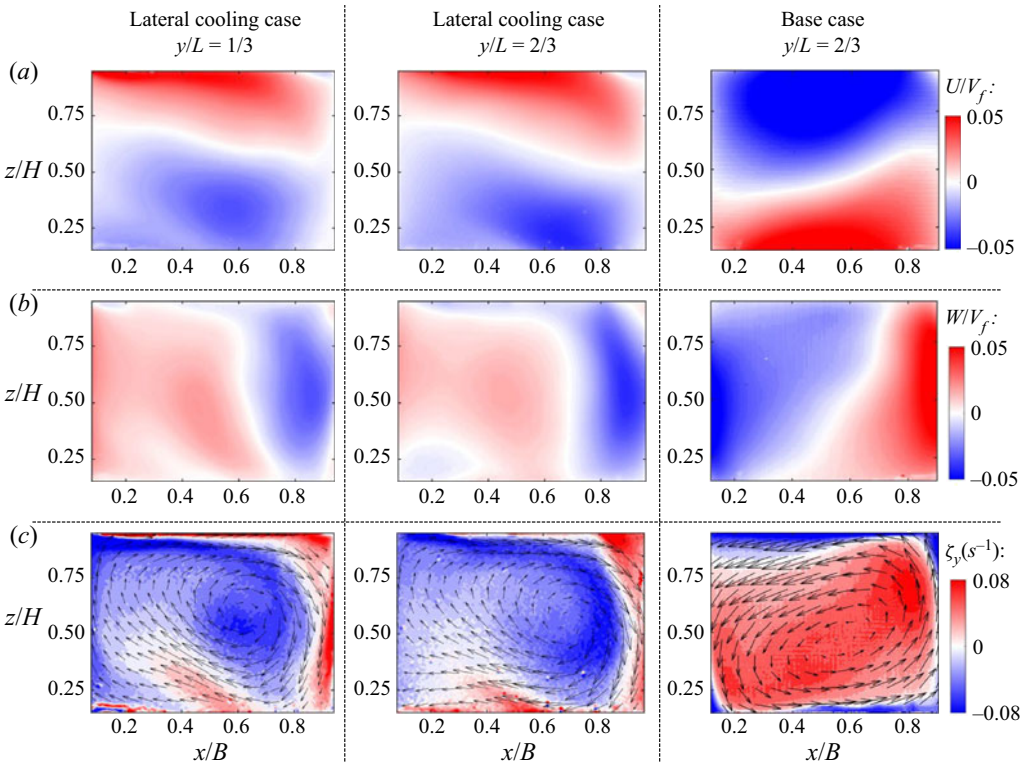

Figure 15. Time-averaged distributions of the (*a*) horizontal and (*b*) vertical velocity fields, and (*c*) vorticity contours with superimposed in-plane velocity vector fields for RB convection with lateral cooling at $Ra = 2 \times 10^9$ and the canonical counterpart (base case).

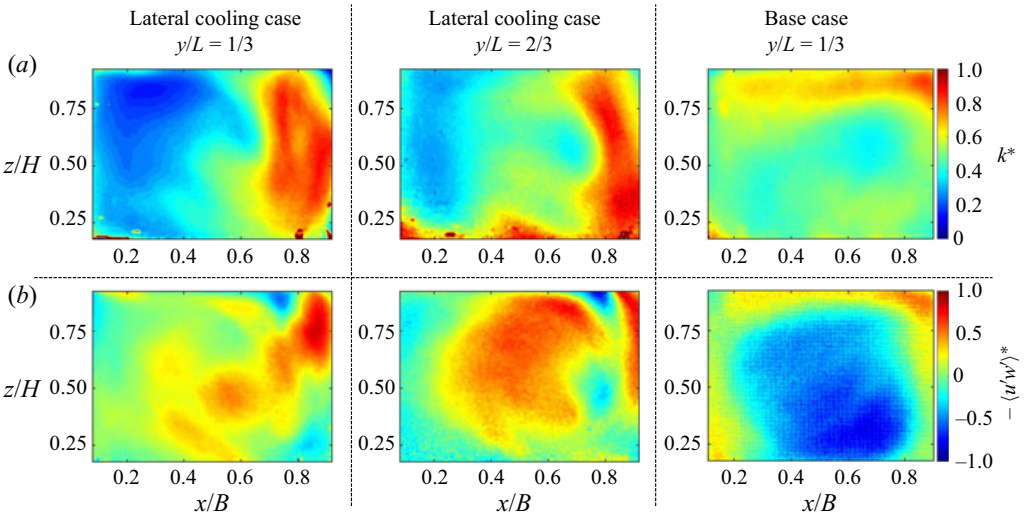

Figure 16. In-plane (*a*) turbulent kinetic energy and (*b*) Reynolds stress for RB convection with lateral cooling and the canonical counterpart at $Ra = 2 \times 10^9$. The values are normalized by their respective maximum.

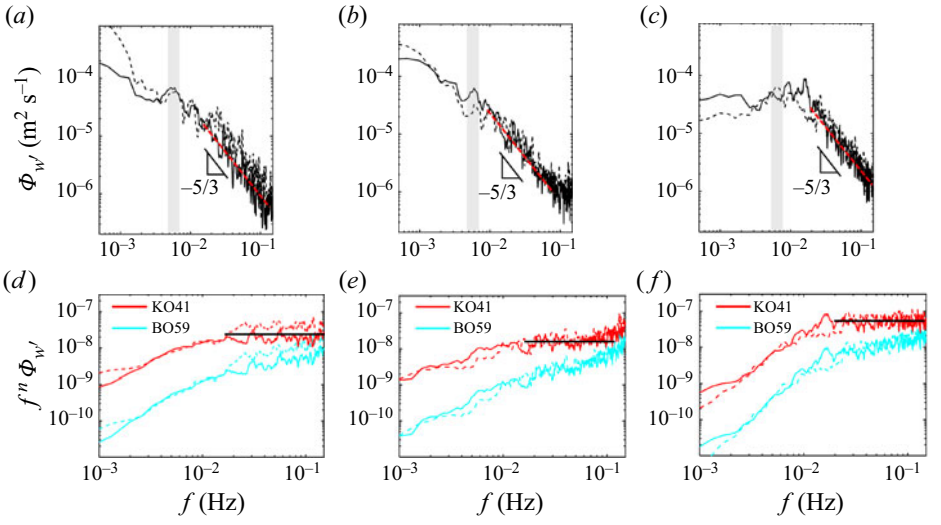

Figure 17. (*a–c*) Power spectra of vertical velocity fluctuations, $\Phi_{w'}$, (*d–f*) compensated forms $f^{5/3}\Phi_{w'}$ (KO41) and $f^{11/5}\Phi_{w'}$ (BO59) at the vortex core location (solid line) and at $\Delta x/B = 0.2$ from the vortex core in the horizontal direction (dashed line) for the single sidewall cooling $Ra = 2 \times 10^9$ case at (*a*,*d*) $y/L = 1/3$ and (*b*,*e*) $y/L = 2/3$. (*c*,*f*) Canonical counterpart (no sidewall cooling).

Ra (figure 17). However, only the KO41 scaling is dominant, with BO59 scaling no longer observable, suggesting a weaker buoyancy effect at lower *Ra*.

References

Bailon-Cuba, J., Emran, M. & Schumacher, J. 2010 Aspect ratio dependence of heat transfer and large-scale flow in turbulent convection. *J. Fluid Mech.* **655**, 152–173.

Bodenschatz, E., Pesch, W. & Ahlers, G. 2000 Recent developments in Rayleigh–Bénard convection. *Annu. Rev. Fluid Mech.* **32** (1), 709–778.

Bolgiano, R. 1959 Turbulent spectra in a stably stratified atmosphere. *J. Geophys. Res.* **64** (12), 2226–2229.

Brown, E. & Ahlers, G. 2009 The origin of oscillations of the large-scale circulation of turbulent Rayleigh–Bénard convection. *J. Fluid Mech.* **638**, 383–400.

Castaing, B., Gunaratne, G., Heslot, F., Kadanoff, L., Libchaber, A., Thomae, S., Wu, X.Z., Zaleski, S. & Zanetti, G. 1989 Scaling of hard thermal turbulence in Rayleigh–Bénard convection. *J. Fluid Mech.* **204**, 1–30.

Chen, S. & Lavine, A. 1996 Laminar, buoyancy induced flow structures in a bottom heated, aspect ratio 2 duct with through flow. *Intl J. Heat Mass Transfer* **39** (1), 1–11.

Ciliberto, S., Cioni, S. & Laroche, C. 1996 Large-scale flow properties of turbulent thermal convection. *Phys. Rev.* E **54**, R5901–R5904.

Funfschilling, D., Brown, E. & Ahlers, G. 2008 Torsional oscillations of the large-scale circulation in turbulent Rayleigh–Bénard convection. *J. Fluid Mech.* **607**, 119–139.

Hamed, A.M., Sadowski, M.J., Nepf, H.M. & Chamorro, L.P. 2017 Impact of height heterogeneity on canopy turbulence. *J. Fluid Mech.* **813**, 1176–1196.

Horn, S., Schmid, P.J. & Aurnou, J.M. 2021 Unravelling the large-scale circulation modes in turbulent Rayleigh–Bénard convection. *Europhys. Lett.* **136** (1), 14003.

Huang, X.-J., Hu, Y.-P. & Li, Y.-R. 2019 Aspect ratio dependence of Rayleigh–Bénard convection of cold water near its maximum density in box-shaped containers. *Phys. Fluids* **31** (7), 075107.

Huang, S.-D., Wang, F., Xi, H.-D. & Xia, K.-Q. 2015 Comparative experimental study of fixed temperature and fixed heat flux boundary conditions in turbulent thermal convection. *Phys. Rev. Lett.* **115**, 154502.

Ji, D. & Brown, E. 2020 Oscillation in the temperature profile of the large-scale circulation of turbulent convection induced by a cubic container. *Phys. Rev. Fluids* **5**, 063501.

KIM, J., NAM, J., SHEN, S., LEE, C. & CHAMORRO, L. 2020 On the dynamics of air bubbles in Rayleigh–Bénard convection. *J. Fluid Mech.* **891**, A7.

KIM, J., SHEN, S., DIMARCO, S., JIN, Y. & CHAMORRO, L. 2018 Lagrangian acceleration in Rayleigh–Bénard convection at various aspect ratios. *Phys. Rev. Fluids* **3** (11), 113502.

KRISHNAMURTI, R. & HOWARD, L. 1981 Large-scale flow generation in turbulent convection. *Proc. Natl Acad. Sci.* **78** (4), 1981–1985.

OBUKHOV, A. 1959 Effect of archimedean forces on the structure of the temperature field in a turbulent flow. *Dokl. Akad. Nauk SSSR* **125** (6), 1246–1248.

PAOLILLO, G., GRECO, C.S., ASTARITA, T. & CARDONE, G. 2021 Experimental determination of the 3-d characteristic modes of turbulent Rayleigh–Bénard convection in a cylinder. *J. Fluid Mech.* **922**, A35.

PODVIN, B. & SERGENT, A. 2012 Proper orthogonal decomposition investigation of turbulent Rayleigh–Bénard convection in a rectangular cavity. *Phys. Fluids* **24** (10), 105106.

QIU, X.-L., SHANG, X.-D., TONG, P. & XIA, K.-Q. 2004 Velocity oscillations in turbulent Rayleigh–Bénard convection. *Phys. Fluids* **16** (2), 412–423.

QIU, X. & TONG, P. 2001*a* Large-scale velocity structures in turbulent thermal convection. *Phys. Rev.* E **64**, 036304.

QIU, X.-L. & TONG, P. 2001*b* Onset of coherent oscillations in turbulent Rayleigh–Bénard convection. *Phys. Rev. Lett.* **87**, 094501.

RAYLEIGH, LORD 1916 On convection currents in a horizontal layer of fluid, when the higher temperature is on the under side. *Lond. Edinb. Dublin Philos. Mag. J. Sci.* **32** (192), 529–546.

REMPFER, D. & FASEL, H.F. 1994 Evolution of three-dimensional coherent structures in a flat-plate boundary layer. *J. Fluid Mech.* **260**, 351–375.

RINGNÉR, M. 2008 What is principal component analysis? *Nat. Biotechnol.* **26** (3), 303–304.

SAKIEVICH, P.J., PEET, Y.T. & ADRIAN, R.J. 2016 Large-scale thermal motions of turbulent Rayleigh–Bénard convection in a wide aspect-ratio cylindrical domain. *Intl J. Heat Fluid Flow* **61**, 183–196.

SHANG, X. & XIA, K. 2001 Scaling of the velocity power spectra in turbulent thermal convection. *Phys. Rev.* E **64** (6), 065301.

SIROVICH, L. 1987 Turbulence and the dynamics of coherent structures. I. Coherent structures. *Q. Appl. Maths* **45** (3), 561–571.

STEVENS, R., LOHSE, D. & VERZICCO, R. 2014 Sidewall effects in Rayleigh–Bénard convection. *J. Fluid Mech.* **741**, 1–27.

SUGIYAMA, K., *et al.*2010 Flow reversals in thermally driven turbulence. *Phys. Rev. Lett.* **105**, 034503.

VERZICCO, R. 2002 Sidewall finite-conductivity effects in confined turbulent thermal convection. *J. Fluid Mech.* **473**, 201–210.

VOGT, T., HORN, S., GRANNAN, A.M. & AURNOU, J.M. 2018 Jump rope vortex in liquid metal convection. *Proc. Natl Acad. Sci. USA* **115** (50), 12674–12679.

WAGNER, S. & SHISHKINA, O. 2013 Aspect-ratio dependency of Rayleigh–Bénard convection in box-shaped containers. *Phys. Fluids* **25** (8), 085110.

WAN, Z.H., WEI, P., VERZICCO, R., LOHSE, D., AHLERS, G. & STEVENS, R.J.A.M. 2019 Effect of sidewall on heat transfer and flow structure in Rayleigh–Bénard convection. *J. Fluid Mech.* **881**, 218–243.

WANG, Q., LIU, H.-R., VERZICCO, R., SHISHKINA, O. & LOHSE, D. 2021 Regime transitions in thermally driven high-Rayleigh number vertical convection. *J. Fluid Mech.* **917**, A6.

WU, X.Z., KADANOFF, L., LIBCHABER, A. & SANO, M. 1990 Frequency power spectrum of temperature fluctuations in free convection. *Phys. Rev. Lett.* **64**, 2140–2143.

XI, X.H., LAM, S. & XIA, K. 2004 From laminar plumes to organized flows: the onset of large-scale circulation in turbulent thermal convection. *J. Fluid Mech.* **503**, 47–56.

XIA, K., SUN, C. & ZHOU, S. 2003 Particle image velocimetry measurement of the velocity field in turbulent thermal convection. *Phys. Rev.* E **68**, 066303.

YU, C., CHANG, M. & LIN, T. 1996 Linear stability of mixed convection flows in horizontal rectangular channels of finite transversal extension heated from below. *Intl J. Heat Mass Transfer* **39** (1), 1–11.

YU, C.H., CHANG, M.Y. & LIN, T.F. 1997 Structures of moving transverse and mixed rolls in mixed convection of air in a horizontal plane channel. *Intl J. Heat Mass Transfer* **40** (2), 333–346.

ZHANG, S., CHEN, X., XIA, Z., XI, H.-D., ZHOU, Q. & CHEN, S. 2021 Stabilizing/destabilizing the large-scale circulation in turbulent Rayleigh–Bénard convection with sidewall temperature control. *J. Fluid Mech.* **915**, A14.

ZHANG, Y., HUANG, Y., JIANG, N., LIU, Y., LU, Z., QIU, X. & ZHOU, Q. 2017 Statistics of velocity and temperature fluctuations in two-dimensional Rayleigh–Bénard convection. *Phys. Rev.* E **96**, 023105.

ZHOU, Q., XI, H.-D., ZHOU, S.-Q., SUN, C. & XIA, K.-Q. 2009 Oscillations of the large-scale circulation in turbulent Rayleigh–Bénard convection: the sloshing mode and its relationship with the torsional mode. *J. Fluid Mech.* **630**, 367–390.